Journal of Magnetism and Magnetic Materials 564 (2022) 170056

Contents lists available at ScienceDirect

Journal of Magnetism and Magnetic Materials

journal homepage: www.elsevier.com/locate/jmmm

Research article

Design and modelling of a controlled saturable inductor for an LCC-S compensated WPT system

Luigi Solimene [a,*], Fabio Corti [b], Salvatore Musumeci [a], Carlo Stefano Ragusa [a], Alberto Reatti [c], Ermanno Cardelli [b]

[a] Politecnico di Torino, Department of Energy, Corso Duca degli Abruzzi 24, Torino, 10129, Italy
[b] University of Perugia, Department of Engineering, Via G. Duranti 67, Perugia, 06125, Italy
[c] University of Firenze, Department of Information Engineering, Via di Santa Marta 3, Firenze, 50139, Italy

ARTICLE INFO

Keywords:
Wireless power transfer
Magnetic control
Controlled variable inductor

ABSTRACT

This paper analyses the design of a controlled variable inductor adopted as the series inductance of an LCC-S compensation network in an Inductive Wireless Power Transfer system. In this compensation topology, the power transfer to the load can be controlled by varying the differential inductance of the component through a DC bias. The analytical design process of a double E ferrite core variable inductor is presented, and the specifications for an experimental prototype are proposed. The design output is verified with FEM simulations to validate the obtained differential inductance profile and with circuit simulations to test the non-linear behaviour of the component under the typical current and voltage waveforms of the LCC-S compensated Wireless Power Transfer system. Finally, a prototype is realized, characterized and tested in an experimental Wireless Power Transfer system.

1. Introduction

The inductive Wireless Power Transfer (WPT) technology is becoming adopted extensively in battery charger systems, both in low power applications, such as consumer electronics or medical equipment and high power applications, as in the automotive field [1–4]. The wireless solution shows some advantages compared to the wired one, such as the suppression of bulky cables and connectors, which are parts typically exposed to deterioration, and presents a higher comfort for the users [5]. However, the main limitation of inductive WPT systems compared to wired solutions is the conversion efficiency. The high leakage flux caused by the large air gap between coils determines a low coupling coefficient. It involves a high reactive power value, influencing the transmission efficiency of the system. In order to improve efficiency, additional reactive components are adopted to create resonance and ensure maximum power transfer. Several resonant compensation topologies have been proposed over the years [6,7]. The most intuitive choice, and the most widely adopted topology, is the Series-Series (SS) compensation. This configuration consists of two capacitors in series with the transmitter and the receiver coils. However, other solutions, such as LCC-S (LCC-Series), represented in Fig. 1, offer more freedom in the design and regulation of the system, reducing the passive component's voltage/current stress compared with the SS compensation [8]. An accurate power loss comparison between SS and LCC-S is presented in [9]. The results show the higher conversion efficiency of the LCC-S. While the control of the SS compensation is relatively simple since it acts as a current source, the control of the LCC-S compensation is more complex. Most of the control strategies consist of varying a passive component to regulate the output voltage or current. This paper proposes a novel approach to control the resonant series inductance value. This approach is usually defined as magnetic control, and it has been widely adopted for the LLC resonant converter [10–12].

A controlled variable inductor is realized by controlling the permeability of the core material through an auxiliary magnetizing winding supplied by a DC current source. The paper analyses the design of a controlled saturable inductor suitable for an experimental 100 W WPT system. The analytical design process output is verified with FEM simulation to validate the differential inductance profile of the component and with circuital simulations in PLECS®, considering the non-linear characteristic of the variable inductance during the WPT system operation. In conclusion, a test inductor is realized, characterized

* Corresponding author.
E-mail address: luigi.solimene@polito.it (L. Solimene).

https://doi.org/10.1016/j.jmmm.2022.170056
Received 30 May 2022; Received in revised form 24 September 2022; Accepted 7 October 2022
Available online 2 November 2022

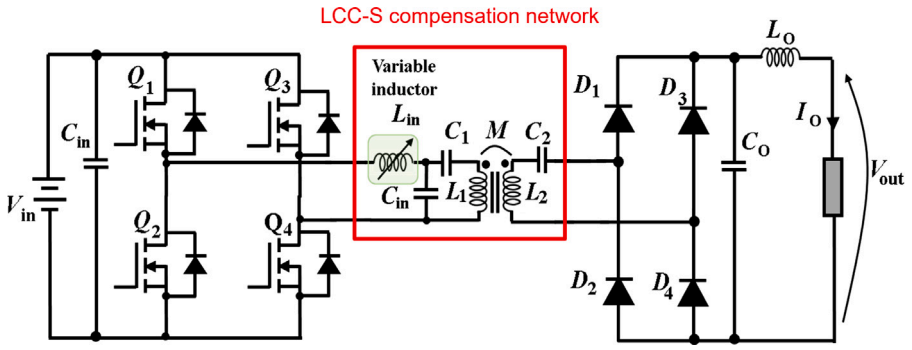

Fig. 1. Equivalent electrical scheme of the LCC-S compensated WPT system. The red box highlights the compensation network.

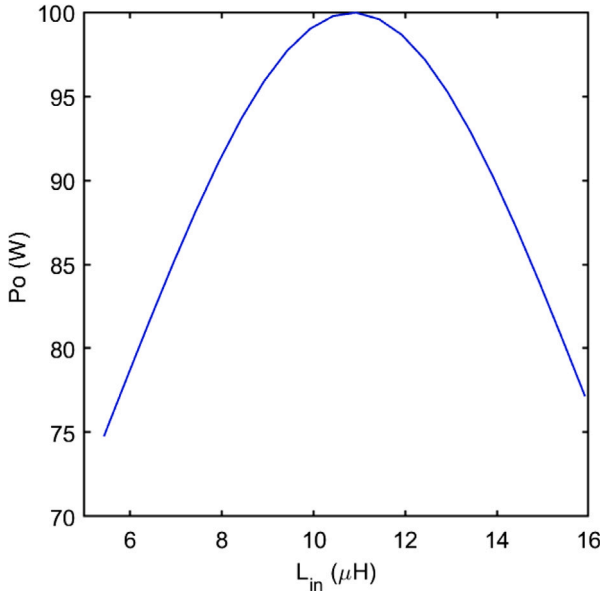

Fig. 2. Profile of the output power as a function of the input inductance L_{in} value, for a 100 W WPT system.

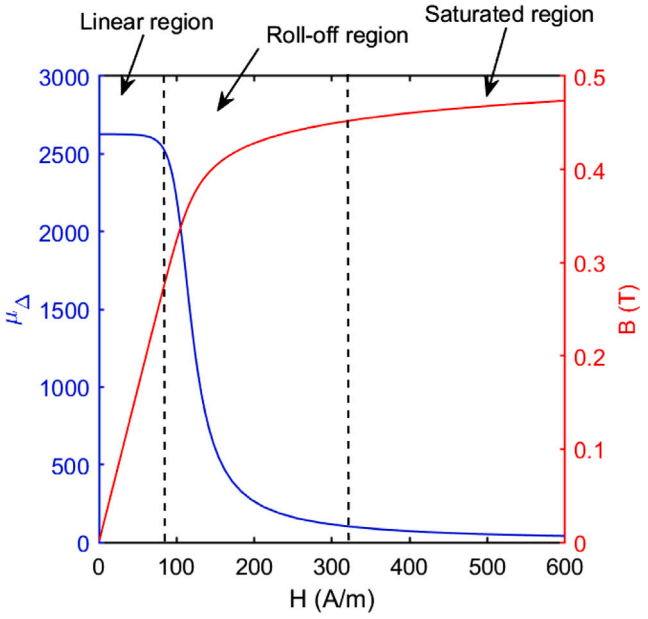

Fig. 3. Magnetization curve and differential permeability profile of the N87 ferrite. The three operating region of the magnetic material are highlighted.

and tested to verify the effectiveness of the design process and adopted in an experimental 100 W WPT system.

2. Preliminary design of the saturable inductor

In an LCC-S compensated WPT system, the input inductance value L_{in} influences the power transferred to the load, as represented in Fig. 2, where the output power profile of a 100 W WPT system is proposed as a function of the input inductance value. A controlled variable inductor, whose inductance can be accurately regulated, allows the active and continuous regulation of the output power [13]. The basic principle of a controlled variable inductor (CVI) is the variation of the permeability of a ferromagnetic material. The differential permeability is defined as the relative permeability corresponding to the slope at a given point on a magnetization curve of magnetic flux density: [14]:

$$\mu_d = \frac{1}{\mu_0}\frac{dB}{dH}. \quad (1)$$

As represented in Fig. 3, which shows a typical differential permeability profile of the N87 ferrite, at low values of the applied magnetic field, the magnetic material operates in a linear region of the magnetization curve, where the differential permeability exhibits a near-constant profile. Under increasing magnetic field, the material tends to operate in the roll-of region of the magnetization curve. The differential permeability value rapidly decreases, going towards the saturation

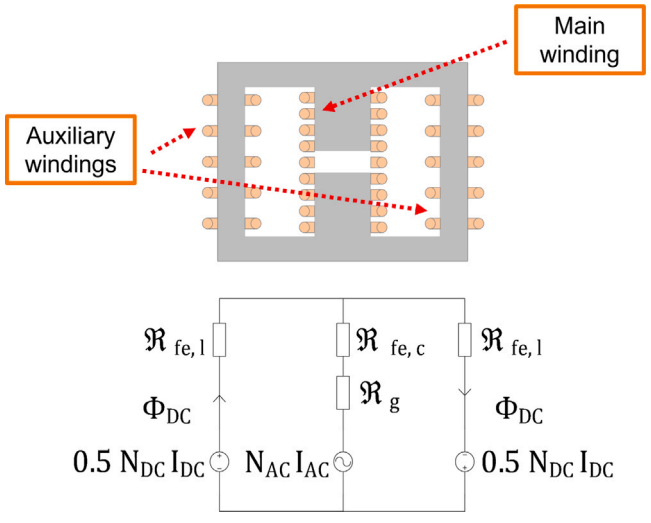

Fig. 4. Description of the core and winding configurations for the controlled variable inductor design and equivalent reluctance circuit.

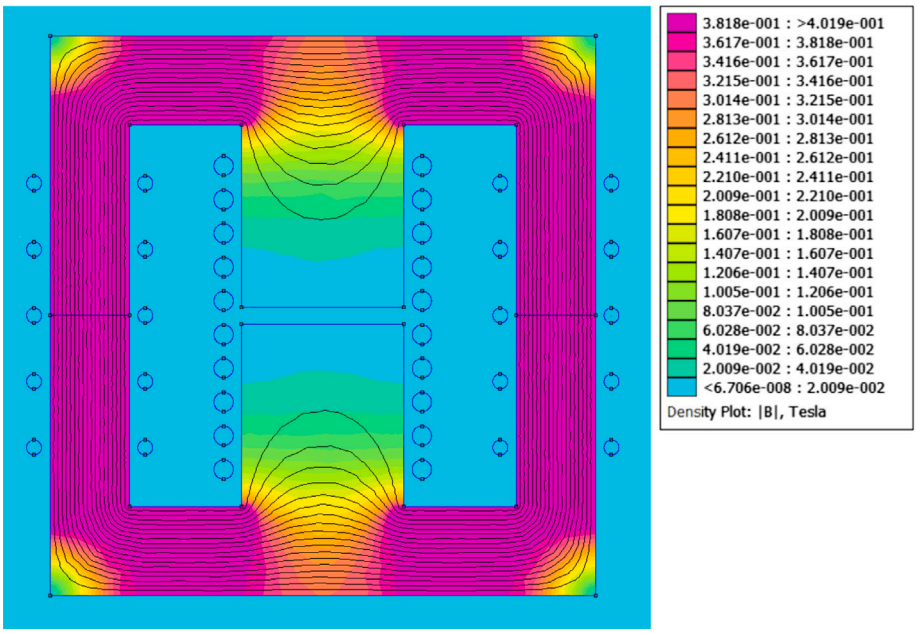

Fig. 5. Magnetic flux density distribution obtained by FEM simulation of the proposes double E core. Only the auxiliary windings on the outer legs are supplied. The DC magnetic flux path involves only the outer legs of the core.

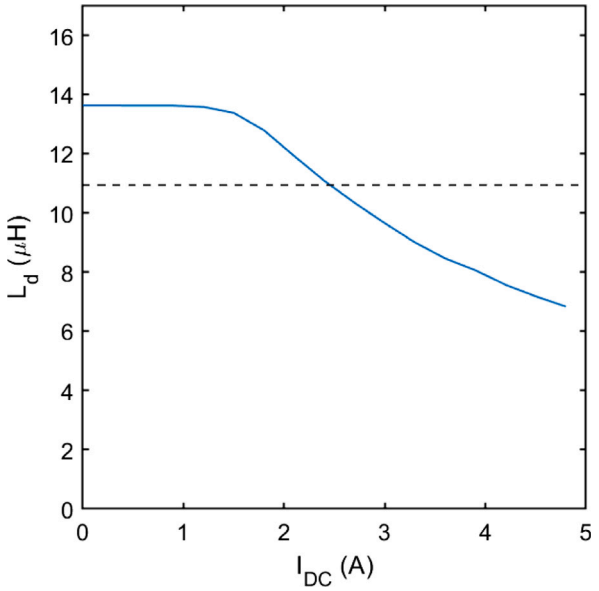

Fig. 6. Differential inductance profile as a function of the magnetizing current, computed with the analytical reluctance model for the prototype defined in Table 2.

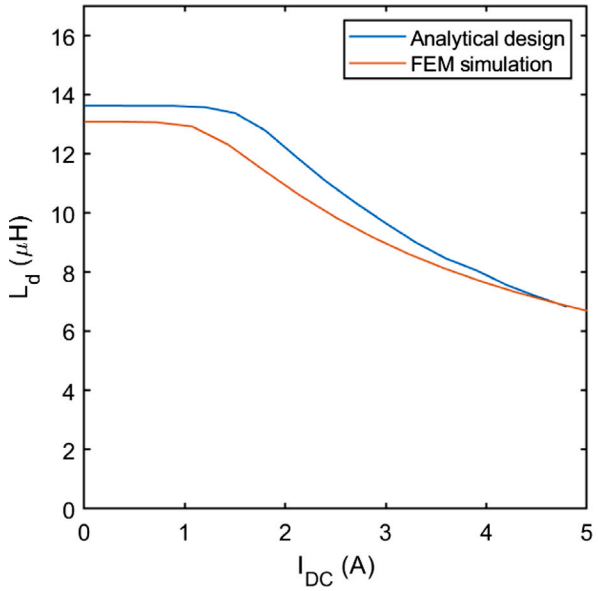

Fig. 7. Comparison of the differential inductance profile obtained with the analytical reluctance model, and the one obtained from FEM simulations.

region, in which the minimum value of the differential permeability is obtained. Considering a closed core shape with an N turns winding, the differential inductance is defined as [15]

$$L_{\mathrm{d}} = \frac{\mathrm{d}\Phi}{\mathrm{d}i}. \tag{2}$$

Assuming the cross-section S is constant over the entire ferromagnetic path, the magnetic flux Φ is defined as

$$\Phi = N\ S\ B. \tag{3}$$

Furthermore, the applied current i is related to the magnetic field H through the Ampere's Law:

$$i = \frac{H\ l_{\mathrm{fe}}}{N}. \tag{4}$$

Thus the differential inductance can be directly related to the differential permeability of the core:

$$L_{\mathrm{d}} = N^2 \frac{S}{l_{\mathrm{fe}}} \frac{\mathrm{d}B}{\mathrm{d}H} = N^2 \frac{S}{l_{\mathrm{fe}}}\ \mu_0\ \mu_d = \frac{N^2}{\mathcal{R}_{\mathrm{eq,d}}}. \tag{5}$$

Considering a double E core geometry, the most suitable solution to obtain a controlled variable inductor is to place the AC winding (connected to the LCC resonant tank) on the central leg of the core. In addition, an auxiliary DC winding is placed on the outer legs to regulate the magnetic field's static value and control the inductance value. The DC winding splits into two windings of 0.5 N_{DC} turns, one on each outer leg, connected in anti-series. In this way, the DC magnetic flux path interest only the core's outer legs, where the differential permeability of the material is controlled through the magnetizing

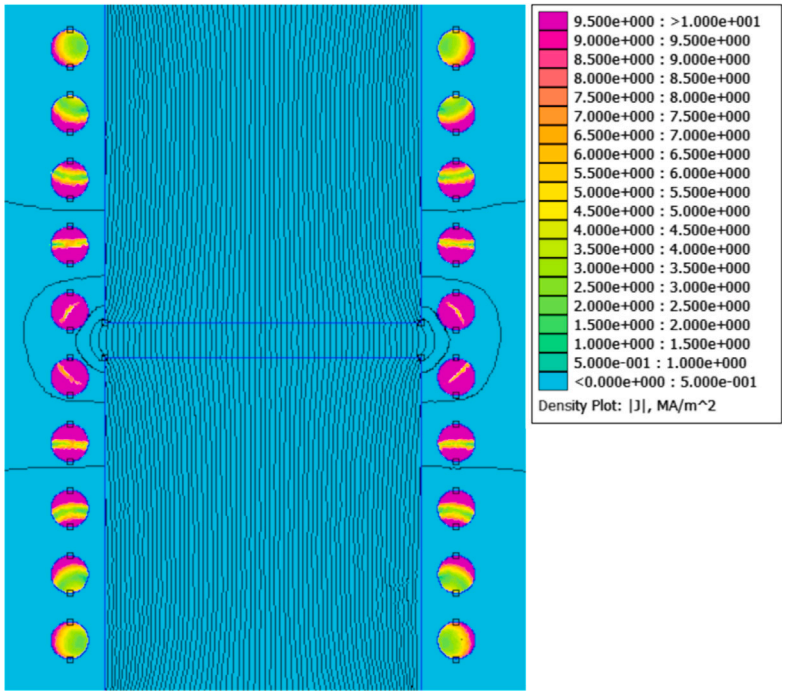

Fig. 8. Current density distribution in the wire of the main winding, at 85 kHz. The conductors in the air gap region are interested by higher current density values.

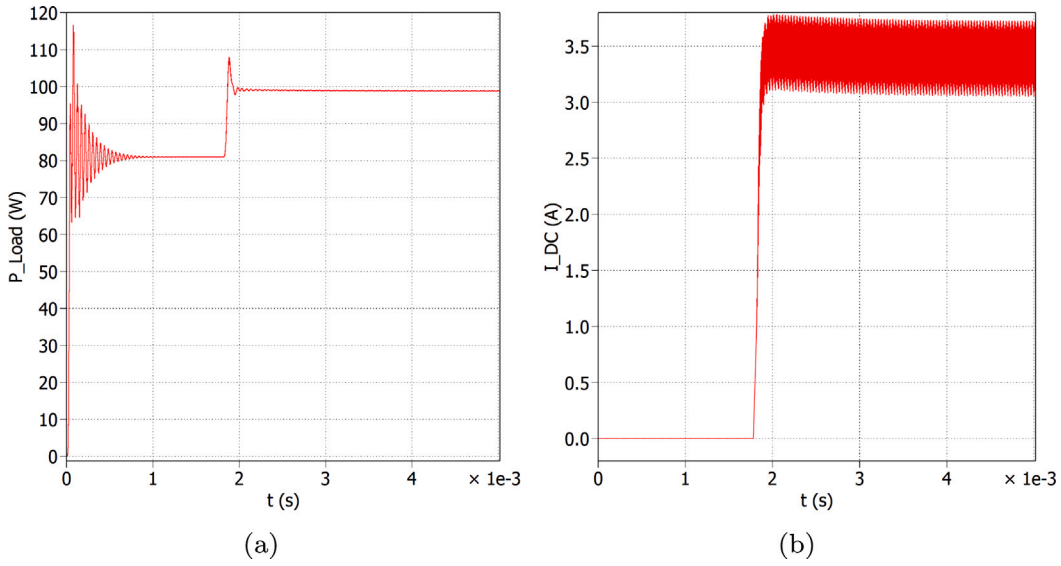

Fig. 9. (a) Average power transferred to the load, in the unsaturated and saturated operation of the controlled variable inductor. (b) Related magnetizing current profile in the auxiliary windings.

current of the auxiliary windings. Due to the resonant behaviour of the considered WPT system, the average magnetic field density in the central leg is zero. Thus, if the amplitude of the AC magnetic field swing is limited, the magnetic material of the central leg's region operates in the unsaturated region [16]. Fig. 5 represents a 2D FEM simulation of the proposed double E core configuration when only the auxiliary windings are supplied. The magnetic flux path and the magnetic flux density colour map highlight how the core's central leg is practically not involved in the magnetic flux applied by the DC windings. An air gap in the central leg is adopted to maintain the magnetic flux density at low values even when the AC winding applies high magnetomotive force values. Moreover, the anti-series connection of the outer leg windings almost cancels the sum of the AC electromotive force on each DC winding. Under the previous assumptions, the equivalent reluctance model represented in Fig. 4 can be adopted to compute the differential inductance profile of the presented core [17,18].

The equivalent differential reluctance, reported in (5) and referred to the AC winding, can be computed as

$$\mathcal{R}_{\mathrm{eq,d}} = \mathcal{R}_{\mathrm{tot,c}} + 0.5\ \mathcal{R}_{\mathrm{tot,l}}, \tag{6}$$

where

$$\mathcal{R}_{\mathrm{tot,c}} = \frac{l_{\mathrm{fe,c}}}{\mu_0\ \mu_{\mathrm{fe,in}}\ S_{\mathrm{fe,c}}} + \frac{l_{\mathrm{g}}}{\mu_0\ S_{\mathrm{g}}} \tag{7}$$

and

$$\mathcal{R}_{\mathrm{tot,l}} = \frac{l_{\mathrm{fe,l}}}{\mu_0\ \mu_{\mathrm{fe,d}}}\ S_{\mathrm{fe,l}}. \tag{8}$$

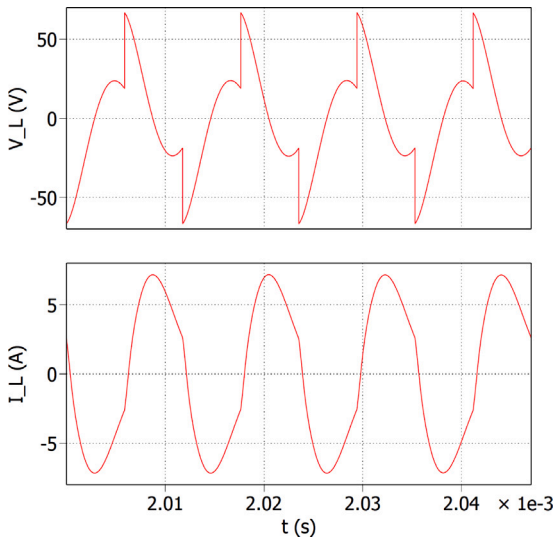

Fig. 10. Typical voltage and current waveforms of the input inductor in the LCC-S compensated WPT system.

Table 1
Specification of the tested WPT system.

Switching frequency	85 kHz
Inductance range	15 μH–10 μH
AC winding current	4.5 A (RMS)

Table 2
Design parameter of the controlled variable inductor prototype.

Core material	N87 ferrite
Core geometry	E 32/16/9
Gap length	1 mm
AC winding N turns	10
DC winding N turns	10 (5 + 5)

$\mu_{fe,in}$, adopted in the computation of the ferromagnetic path reluctance of the central leg in (7), is the initial permeability value of the magnetic material. The differential permeability value $\mu_{fe,d}$, adopted in the computation of the ferromagnetic path reluctance of the outer leg in (8), is a function of the DC magnetomotive force that determines the magnetic field strength. The differential inductance profile can be tuned to regulate the WPT system's power transfer by controlling this parameter.

The gap cross-section S_g of (7) is corrected in order to consider the fringing field's effects on the equivalent gap reluctance, as [19]

$$S_g = (a + l_g) \cdot (b + l_g), \tag{9}$$

where a and b are the two dimensions of the central column cross-section.

The reluctance model has been adopted to compare different core dimensions, gap length values, and numbers of turns on the AC and DC windings, to define a design suitable to the application specification, presented in Table 1.

Table 2 describes the selected material, geometrical and winding parameters of the prototype. Fig. 6 represents the computed differential inductance profile as a function of the applied magnetizing current in the auxiliary windings.

3. Simulation verification of the controlled inductor parameters

3.1. FEM simulation

In order to verify the differential inductance profile of the designed controlled variable inductor, a magnetostatic 2D FEM simulation of the analysed geometry is performed through the software FEMM. Different simulation steps are performed under increasing magnetizing current in the auxiliary windings while the main winding is supplied with a small signal current. As represented in Fig. 7, the FEM simulation output shows overall compatibility with the analytical differential inductance profile. Minor differences can be ascribed to the fringing flux effects due to the air gap and the leakage flux paths not considered in the analytical reluctance model. However, the deviation between the two differential inductance curves is still negligible compared to the tolerances on the permeability value of the material and the geometrical dimensions of the core. In addition, the FEM simulation allows verifying the AC resistance increase of the windings due to the skin and proximity effect. In particular, the goal is to minimize the high-frequency resistance of the main winding, supplied with AC waveforms, that can cause a non-negligible increase of the ohmic losses at 85 kHz. However, the main winding, placed on the central leg of the core, is also subjected to the high magnetic field in the air gap region, which further accentuates the problem, as represented in Fig. 8, where the current density distribution

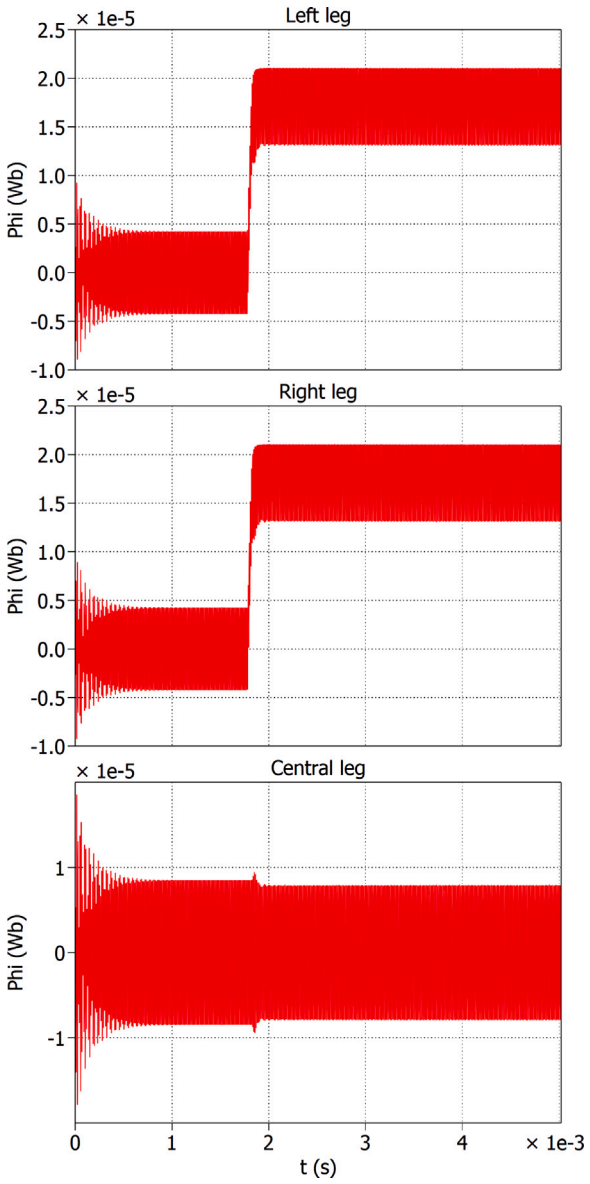

Fig. 11. Magnetic flux waveforms in the three core legs, during the unsaturated and the saturated operation.

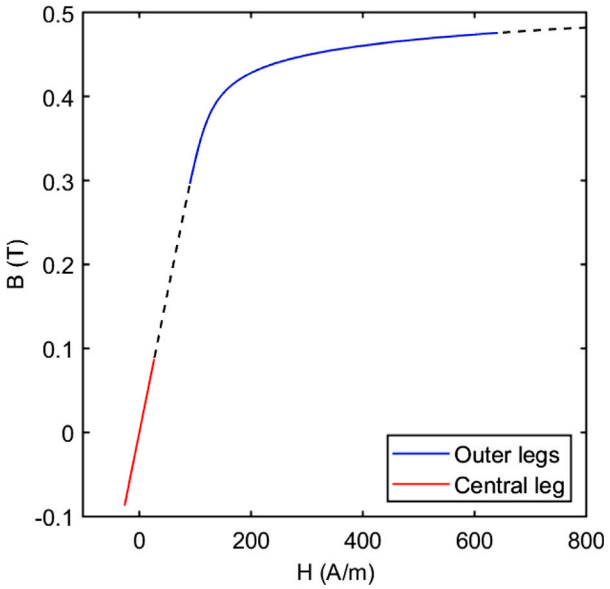

Fig. 12. Operation regions of the magnetic material in the saturated case. The central leg operates in the linear region of the magnetization curve, while the outer legs operate in the roll-off region.

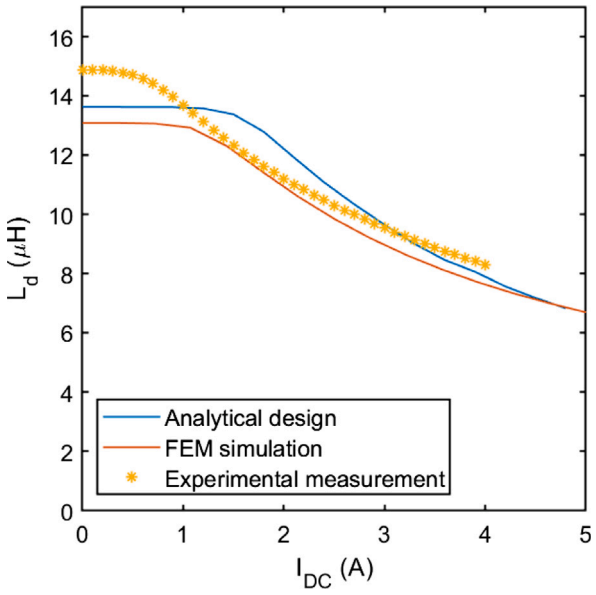

Fig. 13. Measured differential inductance profile of the realized prototype, compared with the analytical reluctance model and the FEM simulation output.

of the AC winding is represented [20]. Considering a winding cross-section of 1 mm^2, the resistance at 85 kHz is 24 times the DC resistance. A practical solution to mitigate the problem is to use litz wire for the main winding. Considering an equivalent 1 mm^2 section made of 130 twisted strands with a diameter of 0.1 mm, the AC over DC resistance ratio reduces to 2.16 without involving an increase in the DC resistance. The high-frequency resistance of the auxiliary winding is not critical because only a reduced AC component can circulate due to the induced electromotive force. For this reason, a solid conductor with a cross-section of 0.6 mm^2 is selected for the auxiliary windings.

3.2. Circuit simulation

In order to verify the operation of the designed variable inductor in the LCC-S compensated WPT system, the software PLECS® is adopted

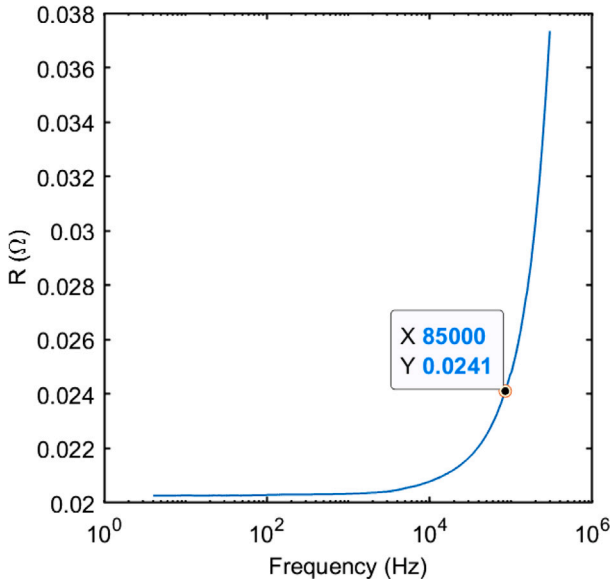

Fig. 14. Measured AC winding resistance as a function of the frequency.

to simulate the entire circuit, taking into account the magnetic model of the inductor. PLECS® allows modelling the magnetic component with a saturable core block, representing the ferromagnetic path reluctance, and an air gap block. The equivalent non-linear reluctance model of the considered double E core can be simulated, considering the interaction with the electrical circuit of the WPT system. Through this simulation, the effectiveness of the designed controllable inductor in the load power transfer control is verified, and the saturation level of each ferromagnetic path under the voltage and current waveforms applied by the LCC-S compensated WPT system is checked. Fig. 9(a) represents the average power transferred to the load in the unsaturated and then in the saturated operation of the controlled variable inductor. In addition, Fig. 9(b) shows the magnetizing current required to saturate the component. The simulation confirms that the load power transfer can be effectively regulated by controlling the auxiliary winding current. Fig. 10 shows the voltage and current waveforms of the inductor during the typical operation of the tested WPT system, and Fig. 11 shows the related magnetic flux swing in the three core legs. Fig. 12 displays the operation regions of the N87 ferrite material when the inductor is saturated. The central leg operates in the linear region of the magnetization curve, while the outer legs operate in the roll-off region.

4. Experimental verification of the design

The controlled variable inductor has been realized following the design specification, and the differential inductance profile and the AC resistance of the main winding are measured. The setup adopted to measure the differential inductance profile as a function of the current of the auxiliary winding is made of the Hioki IM3536 LCR meter, directly connected to the AC winding, and a controllable DC source supplying the magnetizing winding to regulate the magnetizing current. The auxiliary winding circuit should not represent a load for the main windings due to anti-series connection of the two half windings that compensates for the overall induced electromotive force. However, to ensure that the auxiliary winding connections do not influence the measurement, a 2 mH ferrite choke with high saturation current is placed in series with the magnetization circuit. The measurement is performed at 85 kHz. Fig. 13 represents the measured differential inductance profile compared with the analytical reluctance model and the FEM simulation output.

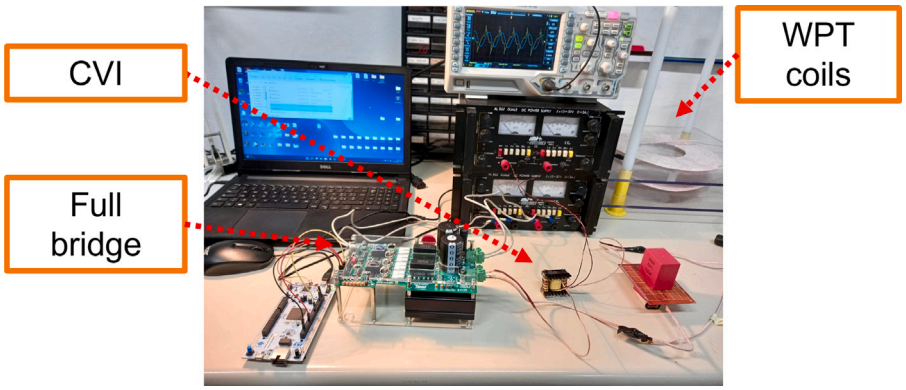

Fig. 15. Photo of the experimental 100W LCC-S compensated WPT system adopted for the test of the controlled variable inductor.

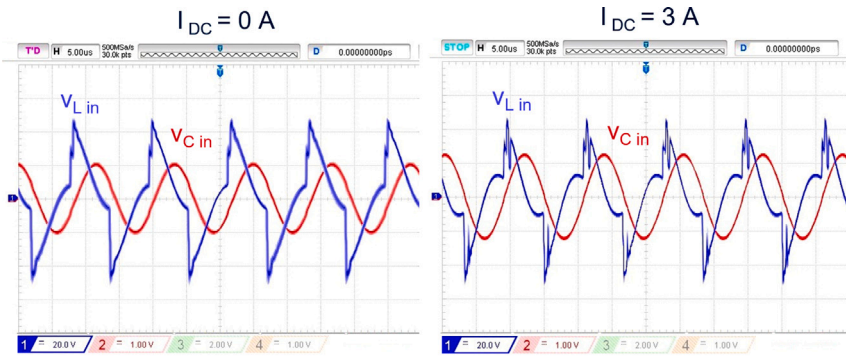

Fig. 16. Measured voltage waveforms on the controlled variable inductor and on the input capacitor. (a) Unsaturated operation. (b) Saturated operation.

As introduced before, the deviations between the experimental differential inductance profile and the simulated ones can be ascribed to the tolerances that the core producer declares on the permeability value, which is defined as ±25% to the nominal values, and the non-negligible but more limited tolerances on the core dimensions and on the gap length. Also, the positioning of the winding on the magnetic core can influence the inductance value of the component and leakage and fringing flux, which are phenomena difficult to model during the design phase. However, the measured differential inductance profile of the realized variable inductor satisfies the requirement of the LCC-S compensated WPT system. In addition, the resistance of the main winding, realized with litz wire, is measured as a function of the frequency to verify the resistive losses at the resonance frequency of the WPT system [21]. The Hioki IM3536 LCR meter is adopted to measure the realized AC winding. The winding, formed over a coil former, is tested without the magnetic core. The so obtained resistance value is underestimated considering the effects of the gapped core on the current density distribution. However, the in-phase current component measured with the winding placed on the cores includes also the contribution of the magnetic losses of the material, which are difficult to separate from the resistive losses of the winding at high frequency. Under this simplification, the measured behaviour of the main winding resistance as a function of the supply frequency is presented in Fig. 14. At the resonance frequency of the WPT system, a 19% increase with respect to the DC resistance is reported in the tested configuration.

5. Test of the experimental WPT system

The controlled variable inductor has been tested during the operation of an experimental LCC-S compensated WPT system. Fig. 15 shows a photo of the experimental setup. The setup is not tested in the full power configuration. The traces of Figs. 16(a) and 16(b) represent the measured voltage waveforms on the controlled variable inductor in the saturated and the unsaturated condition and the voltage applied on the parallel capacitor C_{in} of the LCC-S compensation network. Table 3 describes the transferred load power in the unsaturated and saturated operation of the variable inductor and the required DC current.

Table 3
Measured load power and related magnetization current, for the unsaturated and saturated operation.

	P_{load} (W)	I_{DC} (A)
Unsaturated	34.94	0
Saturated	53.66	3

The experimental results confirm the effectiveness of the load power regulation through the designed controlled variable inductor.

6. Conclusions

The paper proposes the design criteria of an inductor operating under controlled saturation conditions, adopted to realize the magnetic control of the output power in an LCC-S compensated WPT system. First, the specification for a prototype is defined with an analytical procedure, comparing different core dimensions, number of turns and air gap values. Then, the final design configuration is examined with FEM simulations to verify the differential inductance profile and the high-frequency resistance of the main winding. A circuit simulation is also adopted to verify the effectiveness of the designed inductor in the load power transfer regulation and to test the operating point of the different ferromagnetic paths of the core under the typical operation of the WPT system. Finally, a prototype of the designed

controlled variable inductor is realized, characterized and tested in an experimental WPT system, concluding that the magnetic control of the load power is a suitable solution in an LCC-S compensated WPT system. Future works will evaluate the design of the supply circuit for the auxiliary windings and the control strategy of the magnetization current. In addition, the efficiency of the WPT system under different operating conditions has to be analysed, focusing on the inductor losses in the saturated and unsaturated operations.

CRediT authorship contribution statement

Luigi Solimene: Conceptualization, Methodology, Writing – original draft, Writing – review & editing, Investigation, Validation. **Fabio Corti:** Conceptualization, Methodology, Writing – original draft, Writing – review & editing, Investigation, Validation. **Salvatore Musumeci:** Conceptualization, Writing – original draft, Writing – review & editing, Supervision. **Carlo Stefano Ragusa:** Conceptualization, Writing – original draft, Writing – review & editing, Supervision. **Alberto Reatti:** Conceptualization, Writing – review & editing, Supervision. **Ermanno Cardelli:** Conceptualization, Writing – review & editing, Supervision.

Declaration of competing interest

The authors declare that they have no known competing financial interests or personal relationships that could have appeared to influence the work reported in this paper.

Data availability

The data that has been used is confidential.

References

[1] Z. Zhang, H. Pang, A. Georgiadis, C. Cecati, Wireless power transfer—An overview, IEEE Trans. Ind. Electron. 66 (2) (2019) 1044–1058, http://dx.doi.org/10.1109/TIE.2018.2835378.

[2] G. Buja, M. Bertoluzzo, K.N. Mude, Design and experimentation of WPT charger for electric city car, IEEE Trans. Ind. Electron. 62 (12) (2015) 7436–7447, http://dx.doi.org/10.1109/TIE.2015.2455524.

[3] R. Pagano, S. Abedinpour, A. Raciti, S. Musumeci, Efficiency optimization of an integrated wireless power transfer system by a genetic algorithm, in: 2016 IEEE Applied Power Electronics Conference and Exposition, APEC, 2016, pp. 3669–3676, http://dx.doi.org/10.1109/APEC.2016.7468398.

[4] V. Cirimele, M. Diana, F. Freschi, M. Mitolo, Inductive power transfer for automotive applications: State-of-the-art and future trends, IEEE Trans. Ind. Appl. 54 (5) (2018) 4069–4079, http://dx.doi.org/10.1109/TIA.2018.2836098.

[5] C.C. Mi, G. Buja, S.Y. Choi, C.T. Rim, Modern advances in wireless power transfer systems for roadway powered electric vehicles, IEEE Trans. Ind. Electron. 63 (10) (2016) 6533–6545, http://dx.doi.org/10.1109/TIE.2016.2574993.

[6] A. Mahesh, B. Chokkalingam, L. Mihet-Popa, Inductive wireless power transfer charging for electric vehicles–A review, IEEE Access 9 (2021) 137667–137713, http://dx.doi.org/10.1109/ACCESS.2021.3116678.

[7] M. Abou Houran, X. Yang, W. Chen, Magnetically coupled resonance WPT: Review of compensation topologies, resonator structures with misalignment, and EMI diagnostics, Electronics 7 (11) (2018) 296, http://dx.doi.org/10.3390/electronics7110296, URL https://www.mdpi.com/2079-9292/7/11/296, Number: 11 Publisher: Multidisciplinary Digital Publishing Institute.

[8] W. Wang, J. Deng, D. Chen, Z. Wang, S. Wang, A novel design method of LCC-S compensated inductive power transfer system combining constant current and constant voltage mode via frequency switching, IEEE Access 9 (2021) 117244–117256, http://dx.doi.org/10.1109/ACCESS.2021.3105103, URL https://ieeexplore.ieee.org/document/9514598/.

[9] F. Corti, L. Paolucci, A. Reatti, F. Grasso, L. Pugi, N. Tesi, E. Grasso, M. Nienhaus, A comprehensive comparison of resonant topologies for magnetic wireless power transfer, in: 2020 IEEE 20th Mediterranean Electrotechnical Conference, MELECON, 2020, pp. 582–587, http://dx.doi.org/10.1109/MELECON48756.2020.9140657, ISSN: 2158-8481.

[10] Y. Wei, Q. Luo, A. Mantooth, Comprehensive analysis and design of LLC resonant converter with magnetic control, CPSS Trans. Power Electron. Appl. 4 (4) (2019) 265–275, http://dx.doi.org/10.24295/CPSSTPEA.2019.00025.

[11] Y. Wei, Q. Luo, X. Du, N. Altin, J.M. Alonso, H.A. Mantooth, Analysis and design of the LLC resonant converter with variable inductor control based on time-domain analysis, IEEE Trans. Ind. Electron. 67 (7) (2020) 5432–5443, http://dx.doi.org/10.1109/TIE.2019.2934085.

[12] J.M. Alonso, M.S. Perdigão, D.G. Vaquero, A.J. Calleja, E.S. Saraiva, Analysis, design, and experimentation on constant-frequency DC-DC resonant converters with magnetic control, IEEE Trans. Power Electron. 27 (3) (2012) 1369–1382, http://dx.doi.org/10.1109/TPEL.2011.2165083.

[13] L. Solimene, F. Corti, S. Musumeci, C.S. Ragusa, A. Reatti, Magnetic control of LCC-S compensated wireless power transfer system, in: 2022 International Symposium on Power Electronics, Electrical Drives, Automation and Motion, SPEEDAM, IEEE, Sorrento, Italy, 2022, pp. 160–165, http://dx.doi.org/10.1109/SPEEDAM53979.2022.9842241, URL https://ieeexplore.ieee.org/document/9842241/.

[14] British Standards Institution, British Standards Institution, Glossary of Electrotechnical, Power, Telecommunication, Electronics, Lighting and Colour Terms. Part 1. Group 07. Part 1. Group 07., British Standards Institution, London, 1991, OCLC:958836520.

[15] International Electrotechnical Commission, Power Transformers - Part 6, Reactors=Transformateurs de Puissance - Partie 6, Bobines D'Inductance, International Electrotechnical Commission, Geneva, 2007, OCLC:500739001.

[16] J.M. Alonso, M. Perdigão, M.A. Dalla Costa, S. Zhang, Y. Wang, Variable inductor modeling revisited: The analytical approach, in: 2017 IEEE Energy Conversion Congress and Exposition, ECCE, 2017, pp. 895–902, http://dx.doi.org/10.1109/ECCE.2017.8095880.

[17] S. Musumeci, L. Solimene, C.S. Ragusa, Identification of DC thermal steady-state differential inductance of ferrite power inductors, Energies 14 (13) (2021) 3854, http://dx.doi.org/10.3390/en14133854, URL https://www.mdpi.com/1996-1073/14/13/3854.

[18] L. Solimene, C. Ragusa, S. Musumeci, O.d.l. Barrière, F. Fiorillo, Modeling of saturable inductors for application in DC-DC Converters, in: 2019 26th IEEE International Conference on Electronics, Circuits and Systems, ICECS, 2019, pp. 839–842, http://dx.doi.org/10.1109/ICECS46596.2019.8964948.

[19] N. Mohan, T.M. Undeland, W.P. Robbins, Power Electronics: Converters, Applications, and Design, third ed., John Wiley & Sons, Hoboken, NJ, 2003.

[20] W.G. Hurley, M.C. Duffy, J. Acero, Z. Ouyang, J. Zhang, 17 - Magnetic circuit design for power electronics, in: M.H. Rashid (Ed.), Power Electronics Handbook, fourth ed., Butterworth-Heinemann, 2018, pp. 571–589, http://dx.doi.org/10.1016/B978-0-12-811407-0.00019-2.

[21] K. Niyomsatian, J.J.C. Gyselinck, R.V. Sabariego, Experimental extraction of winding resistance in Litz-wire transformers—Influence of winding mutual resistance, IEEE Trans. Power Electron. 34 (7) (2019) 6736–6746, http://dx.doi.org/10.1109/TPEL.2018.2876310.